Energy Equip. Sys./ Vol. 14/No. 1/March 2026/ 57-79

ENERGY EQUIPSYS

Energy Equipment and Systems

www.energyequipsys.com

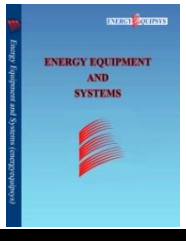

Synergistic flow control via concave vortex generators and magnetic fields: Impacts on flow structure, thermal performance, and irreversibilities

Manuscript Type
Research Paper

Authors

Ali Jalayeri[a]*
Sahar Soleymani[b]
Hadi Barjini Khabbaz[c]

[a] Department of Mechanical Engineering, Urmia University of Technology, Urmia, Iran.

[b] Department of Industrial Engineering, Padua University, Padova, Italy.

[c] Department of Mechanical Engineering, Eqbal Lahoori Institute of Higher Education, Mashhad, Iran.

Article history:
Received: 7 May 2025
Revised: 20 August 2025
Accepted : 15 October 2025

ABSTRACT

This work presents a numerical investigation of ferrofluid flow in a heat exchanger using computational fluid dynamics (CFD) based on the finite volume method (FVM) in ANSYS Fluent. Two flow control techniques are examined: the vortex generator (VG) and the magnetic field (MF) as the Passive and Active flow control methods, respectively. The analysis considers the effects of VG, Reynolds number (Re), angle of attack (α), and the dimensionless magnetic number (Mn), which represents MF intensity. Results indicate that employing the vortex generator (VG) as the sole enhancement method increases heat transfer by 39%, while the MF applied independently achieves a 65% increase. When the two methods are combined, however, they act synergistically, delivering an enhancement of up to 184%. Moreover, at constant Mn, raising the Re reduces the heat transfer rate, and the maximum enhancement of 215% observed at Re = 500 and Mn = 10^{10}. Changing the α alters the thermal behaviour of the vortex structures through enhancing fluid mixing and reducing thermal boundary layers, with optimal heat transfer achieved at 45° and Mn = 7.5×10^{9}. Entropy generation analysis confirms that through the dominance of heat transfer over the friction factor, irreversibility is minimized, with reductions of up to 26%. Overall, the study demonstrates that integrating active and passive flow control methods supported by validated CFD simulations can simultaneously boost heat transfer and reduce entropy, offering an effective strategy for designing compact, high-performance heat exchangers.

Keywords: Flow Control, Vortex Generator, Convective Heat Transfer, Magnetic Field, Entropy.

1. Introduction

In recent years, various flow control strategies [1] such as magnetohydrodynamic (MHD) and ferrohydrodynamic (FHD) techniques [2] [2,3] as well as the use of vortex generators (VGs) [4], have attracted considerable attention for enhancing thermal performance in internal flows. The application of magnetic fields enables active control of the flow structure through Lorentz or Kelvin body forces, which can suppress or promote vortical motions depending on field intensity and configuration. Conversely, VGs act as passive control devices that generate longitudinal vortices, intensify mixing, and delay boundary layer separation. These active and passive approaches

* Corresponding author: Ali Jalayeri
Department of Mechanical Engineering, Urmia University of Technology, Urmia, Iran.
Email: ali_jalayeri@mee.uut.ac.ir

significantly influence heat transfer characteristics, entropy generation, and the distribution of irreversibilities, providing effective tools for optimizing energy efficiency and thermal management in engineering systems [5].

These methods can be broadly categorized into active (AFC) and passive (PFC) flow control techniques [6]. Active flow control involves the use of external energy to modify the flow, such as actuators [7], jets [8], blow and suction [9], or magnetic fields (MF) [10]. These methods allow for real-time adjustments and precise control over flow behaviour, making them highly effective but often more complex and energy-intensive. Examples include plasma actuators, synthetic jets, or MFs in MHD or FHD applications. In contrast, AFC methods do not require external energy to manipulate the flow [11]. Common passive techniques include the use of VGs [12], surface roughness [13], and ribbed walls [14], which induce turbulence or enhance fluid mixing to improve heat transfer or aerodynamic performance. Both techniques are widely used in engineering applications such as heat exchangers [15], combustion systems [16], and aerodynamic surfaces [17,18], where the choice between active and passive control depends on the specific performance goals, complexity, and energy considerations of the system.

The application of MFs as an AFC method has gained attention in fluid dynamics and heat transfer due to their ability to influence conductive fluids. This flow control mechanism can enhance heat transfer by promoting better fluid mixing. In heat exchanger systems, MFs can improve the efficiency of heat transfer processes, especially in systems dealing with conductive fluids. In the following, some of the newest research studies are provided about the effect of MF on thermal systems.

Afifi et al. [19] numerically investigated the combined effects of thermal radiation, thermal conductivity, and variable viscosity on ferrofluid flow through a porous medium in the presence of an MF. The key findings indicate that the presence of the MF suppresses fluid flow, leading to a decrease in the velocity of the ferrofluid. Parametric analysis reveals that a higher MF strength results in a 20-30% reduction in flow velocity, while thermal radiation and thermal conductivity contribute to a 10-15% increase in heat transfer rates. The heat flux and heat source/sink effects on heat transfer in a ferrofluid ($CoFe_2O_4$-H_2O) flow within a horizontal channel under the influence of an induced MF are conducted by Negi et al. [20]. They investigated the effects of different parameters, such as the Hartmann number (Ha), on flow characteristics and heat transfer performance. Results indicate that increasing the MF strength (Ha) reduces the fluid velocity and enhances heat transfer. Magdy et al. [21] analyzed the impact of a non-uniform MF on unsteady heat transfer. The results reveal that the nonuniform MF significantly affects the skin friction and heat transfer coefficients. Moreover, they showed that with higher Prandtl numbers and stronger nonuniform MFs, heat transfer and skin friction increase by 12% and decrease by 15%, respectively. Vortex flow properties and enhanced heat transfer analysis in a curved pipe under MF force are presented by Wnag et al. [22]. The results reveal that applying an MF significantly alters the vortex structure and enhances heat transfer efficiency, with heat transfer rates increasing by up to 25% compared to non-magnetic cases. Meiying et al. [23] presented an experimental investigation into the thermal performance regulation of a composite phase change material (PCM) system influenced by a non-uniform MF generated by a Helmholtz coil. Results demonstrate that applying an MF significantly improves the heat transfer rates during melting and solidification processes. Specifically, the system exhibits up to a 25% reduction in melting time and a 20% increase in heat flux at the highest field strength. The MF enhances the thermal conductivity of the composite PCM, effectively regulating its thermal performance. The experimental study conducted by Ramezani et al. [24] investigates the transient pool boiling heat transfer of deionized water under the influence of an alternating MF (AMF). The effects of different MF intensities, frequencies, and heat fluxes on the heat transfer coefficient were analyzed, and it was shown that the HTC increased by up to 18% as MF strength. An experimental

investigation was conducted by Mansouri et al. [25] to assess the effect of rotating magnetic turbulators on convective heat transfer and pressure drop in a circular tube. The study involved varying Reynolds numbers, MF strengths, and rotation speeds of the magnetic turbulators. Results showed that the rotating magnetic turbulators significantly enhanced the convective heat transfer coefficient by up to 40% compared to the smooth tube baseline. However, this enhancement came with a penalty in pressure drop, which increased by 25% to 60%, depending on the tabulator's rotation speed and MF strength. Benam et al. [26] investigated the saturated flow boiling heat transfer of deionized water and ferrofluids on structured surfaces in an external MF. Experiments were conducted across various heat fluxes and MF intensities to assess their effects on heat transfer performance. The results reveal that ferrofluids and an external MF significantly enhance the heat transfer coefficient compared to deionized water alone. Specifically, the heat transfer coefficient increased by up to 30% under the influence of an MF at 300 kW/m².

VGs are PFC elements widely used in thermal and fluid systems to enhance performance by improving heat transfer and controlling flow behavior. In heat exchangers, VGs are typically employed to augment convective heat transfer by inducing turbulence and disrupting the thermal boundary layer [27]. The vortices caused by VGs improve fluid mixing and promote higher convective heat transfer rates. Therefore, the design of VGs must balance maximizing heat transfer, minimizing pressure drop penalties, and reducing entropy generation to optimize system performance.

An experimental and numerical study was conducted by Liang et al. [28] to investigate the enhanced heat transfer and exergy performance of a heat exchanger equipped with VGs. The impact of VG configurations, including size, shape, and positioning, on the thermal and exergy efficiencies. Results showed that including VGs improves heat transfer rates by 15-35%. The exergy destruction was reduced by 10-25%, and overall exergy efficiency improved by up to 20%. Ifraj et al. [29] investigated the thermal-hydraulic performance enhancement and entropy generation minimization of a heat exchanger utilizing fidget spinner-shaped vortex generators (FSVGs). Experiments and numerical simulations were conducted to evaluate the effects of different FSVG geometries, Reynolds numbers, and VG arrangements on the heat transfer rate and pressure drop. Results indicate that using FSVGs significantly improves the Nusselt number (Nu) and heat transfer coefficient (HTC), with Nu increasing by up to 35% compared to the baseline. However, the associated pressure drop led to a 15% increase in the friction factor. The performance evaluation criterion (PEC) showed an optimal enhancement of 1.2. In another study by Perng et al. [30], the thermo-hydraulic performance enhancement in a round tube using a twisted-staggered concave/convex dimples tape as a passive heat transfer augmentation technique is investigated. Experiments were conducted to evaluate the effects of the dimple tape on heat transfer and friction factor under different Reynolds numbers. The results revealed that using the twisted-staggered concave/convex dimple tape significantly increased the Nusselt number (Nu) and the friction factor (f) compared to a smooth tube. The Nusselt number enhancement varied between 1.5 and 3.2 times that of a smooth tube, depending on the Reynolds number, while the friction factor increased by a factor of 1.8 to 4.0. A numerical investigation was performed to study turbulent forced convection in a square duct heat exchanger (SDHX) equipped with combined vortex turbulators (CVT). The study analyzed the effects of CVT configurations on heat transfer performance and flow characteristics. It revealed that the introduction of CVTs significantly enhanced heat transfer, with the Nusselt number increasing by up to 60% compared to a smooth duct. Pressure drops and penalties associated with CVTs were also evaluated, showing an increase in friction factor by 2.5–4 times relative to the smooth duct [31].

In the context of laminar and steady-state flow, several gaps remain in the CFD-based research of heat transfer enhancement in heat exchangers using VGs and magnetic fields.

Firstly, most existing studies focus on turbulent or unsteady regimes, leaving a limited understanding of how these enhancement techniques behave in low Reynolds number flows, where flow separation and mixing are inherently weaker. The interaction mechanisms between induced vortices and thermal boundary layers in laminar regimes are not fully characterized, particularly concerning different VG shapes, orientations, and placements. Similarly, for magnetic fields, accurate modeling of MHD or FHD effects under steady-state laminar conditions is underexplored. Moreover, the combined effects of VGs and magnetic fields in laminar flow are rarely studied, despite their potential to compensate for the naturally lower convective heat transfer. Addressing these gaps is important for improving heat exchanger performance in applications where laminar flow dominates, such as in microchannel devices, biomedical systems, and compact electronic cooling systems, enabling more efficient and tailored thermal management solutions.

The primary innovation of this study lies in the synergistic integration of two contrasting flow control strategies, magnetic field application as an active technique and vortex generators as a passive technique, within steady laminar ferrofluid flow, a domain that has received limited attention in the literature. While most prior investigations have focused either on magnetic fields under turbulent or transient conditions or on vortex generator applications in conventional fluids at higher Reynolds regimes, this research demonstrates through computational fluid dynamics (CFD) modeling how the combination of these mechanisms can overcome the inherent limitations of laminar flows, namely weak mixing and thick thermal boundary layers. Moreover, the study systematically explores the influence of key governing parameters, including Reynolds number, vortex generator attack angle, and magnetic field intensity (magnetic number), not only on heat transfer enhancement but also on entropy generation and the mitigation of thermodynamic irreversibilities. This dual-perspective analysis, addressing both first-law metrics such as Nusselt number and pressure drop, and second-law considerations through entropy generation, establishes the novelty of the work as extending beyond simple heat transfer improvement. Consequently, the proposed methodology provides a scientifically rigorous and practically viable pathway for the design of compact and high-performance heat exchangers, electronic cooling systems, and biomedical devices, where spatial constraints and laminar flow regimes dominate..

Nomenclature

B	Magnetic flux (Gauss)
C_P	Specific heat (J/Kg. K)
D_h	Hydraulic diameter (m)
Ec	Eckert number (-)
f	Fanning friction factor (-)
H	Magnetic field intensity (A/m)
I_{sec}	Secondary flow intensity (-)
k	Thermal conductivity (W/m. K)
Mn	Magnetic number (-)
Nu	Average Nusselt number (-)
P^*	Non-dimensional pressure (-)
Pe	Peclet number (-)
PEC	Thermal performance coefficient (-)
Pr	Prandtl number (-)
q^*	Non-dimensional heat flux (-)
Re	Reynolds number (-)
S^*	Non-dimensional entropy generation (-)
T^*	Non-dimensional temperature (-)

2. Problem Definition

A three-dimensional channel with H = 4mm, W = 3H, and L = 20H with a pair of concave VGs is shown in Fig. 1. The curvature angle of VG is set to $\beta = 60°$. A magnetic source caused by a wire is located ($X_w/H = 1.5$, $Y_w/H = -0.25$) underneath the bottom wall along the Z-axis. The magnetic field in this study is assumed to be generated by a current-carrying wire, a physically feasible configuration based on Ampère's law. Such an arrangement is widely used in experimental setups and microfluidic systems, providing a controllable and localized magnetic field suitable for ferrofluid applications. The details regarding the VG geometries are listed in Table 1 [32].

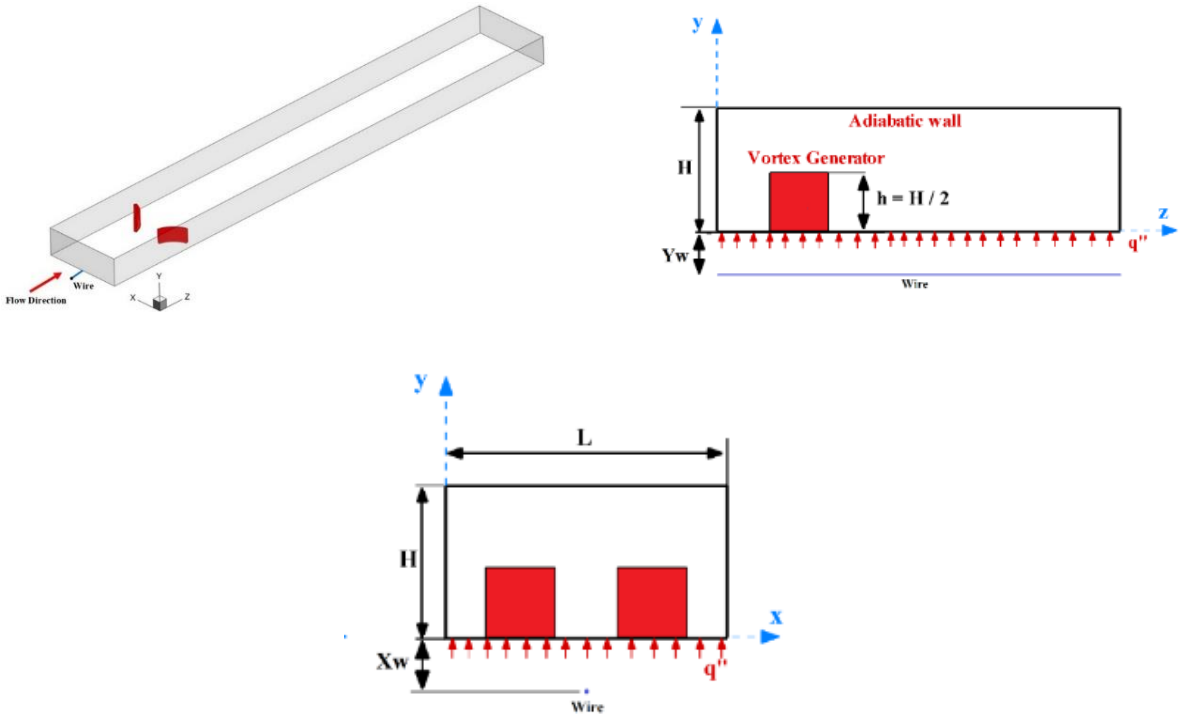

Fig.1. The details geometry of the concave VGs and their formation in the channel

Table 1. Geometrical details of the VG

l/H	t/H	a/H	b/H
1	0.1	1	3

3. Governing Equations

This study considers a laminar, steady-state, incompressible, and Newtonian fluid flow. The influences of radiation, magnetocaloric effects, and gravity are neglected. Given the small temperature variations in the ferrofluid flow and the fact that the Kelvin force is significantly greater than the magnetocaloric force in this study, the latter can be reasonably neglected. Furthermore, within the investigated Reynolds number range, the single-phase modeling approach demonstrates excellent accuracy and shows strong agreement with the corresponding two-phase solutions. In this regard, a homogeneous single-phase model is employed to investigate the impact of magnetic fields on the forced convection of Fe_3O_4–water ferrofluid because of the equilibrium of hydrodynamic and thermal effects of the base fluid and nanoparticles. The volume fraction of the nanoparticles is 2%. The governing equations, in their non-dimensional form, which are obtained from [33,34], are presented as follows:

$$\nabla^* . V^* = 0 \tag{1}$$

$$\rho_{ff} / \rho_{bf} \nabla^* .(V^* V^*) = -\nabla^* P^* + \Pr \nabla^* .(\mu_{ff} / \mu_{bf} \nabla^* V^*) + MnM^* \nabla^* H^* \tag{2}$$

$$(\rho c_p)_{ff} / (\rho c_P)_{bf} V^* .\nabla^* T^* = -\nabla^* P^* + \nabla^* .(k_{ff} / k_{bf} \nabla^* T^*) + \mu_{ff} / \mu_{bf} (\mathrm{Ec}/\mathrm{Pr}) \phi_v^* \tag{3}$$

A uniform MF caused by a current-carrying wire influences the ferrofluid flow shown in Fig. 2. The fx and fy indicate Kelvin forces in the x and y directions. To calculate MF intensity (H) and magnetization (M), the following equations are [34]:

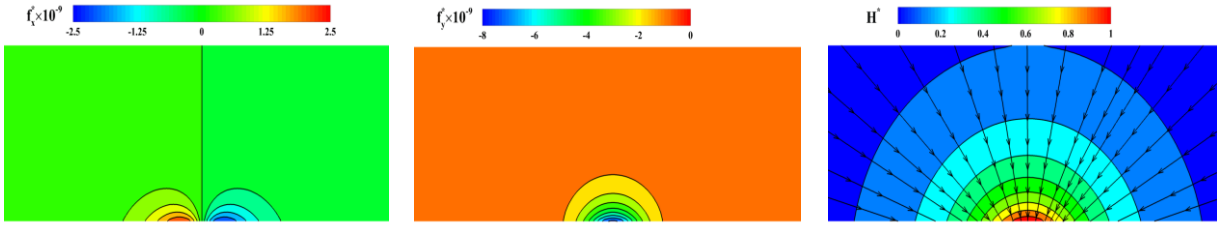

a b c

Fig. 2. Distribution of Kelvin forces and MF intensity

$$H^{*}=H(x,y)/H_0=\left(H_x^2+H_y^2\right)^{0.5}\Big/H_0=\frac{1}{H_0}\left(\left[\sum_{i=1}^{N}\frac{I}{2\pi}\frac{y-y_{w,i}}{(x-x_{w,i})^2+(y-y_{w,i})^2}\right]^2+\left[\sum_{i=1}^{N}\frac{-I}{2\pi}\frac{x-x_{w,i}}{(x-x_{w,i})^2+(y-y_{w,i})^2}\right]^2\right)^{0.5} \quad (4)$$

$$H_0=H(3H/2,0)$$

$$M^{*}=M/M_0=\frac{8.92\times10^{10}}{M_0}\left(\coth\left[3.32\times10^{6}\frac{H^{*}H_0}{300\left(T^{*}q^{*}+1\right)}\right]-1.343\times10^{6}\frac{300\left(T^{*}q^{*}+1\right)}{H^{*}H_0}\right) \quad (5)$$

$$M_0=M(H_0,T_{in})$$

4. Numerical Method

The numerical solution of the governing equations was carried out using the finite-volume method (FVM) implemented in ANSYS Fluent. To ensure both accuracy and stability, the diffusion terms were discretized by the central difference scheme, while the advection terms were treated using a second-order upwind scheme. Pressure–velocity coupling was achieved through the SIMPLE algorithm, which is well-suited for incompressible laminar flows [35]. In addition, a user-defined function (UDF) was developed and integrated into the solver to incorporate the Kelvin force arising from the interaction between the external magnetic field and the ferrofluid magnetization. This UDF modifies the momentum and energy equations to account for the local distribution of magnetic forces, thereby allowing for precise evaluation of the influence of magnetic field intensity and position (as defined in Eqs. 4–5 of this study). The Gauss–Seidel iterative technique combined with an algebraic multigrid (AMG) approach was used to accelerate convergence. A strict convergence criterion of 10^{-7} was imposed on all governing equations, ensuring numerical reliability across the wide range of parameters investigated, including Re, Mn, and α.

5. Ferrofluid Flow Thermal Properties

The properties of ferrofluid flow are expressed using the following equations [36].

In the mentioned equations, B [Gauss] indicates the magnetic flux, and T [oC] is the temperature. Table 2 refers to the thermal properties of the base fluid and nanoparticles.

$$\rho_{ff}=\varphi\rho_{fp}+(1-\varphi)\rho_{bf} \quad (6)$$

$$(\rho c_P)_{ff}=\varphi(\rho c_P)_{fp}+(1-\varphi)(\rho c_P)_{bf} \quad (7)$$

$$\mu_{ff}=\left(\exp\left[-0.02(T+273.15)\times\left(3.5\times10^{4}B^{2}+0.31B-27886.48\varphi^{2}+4263.02\varphi+316.06\right)\right]\right)\Big/1000 \quad (8)$$

$$k_{ff}=\left(1+0.58\varphi^{0.6158}(10^{2}B)^{1.02}\right)\left(1+\varphi+119.22\varphi(T/20)^{0.06423}\right)k_{bf} \quad (9)$$

Table 2. Thermophysical properties of the base fluid and ferroparticles

	Phase	
	Base fluid	**Ferroparticles**
ρ (kg/m^3)	997.1	5180
k (W/m.K)	k_{bf}	80.4
c (J/kg.K)	4197	670
$\mu \times 10^5$ (Pa.s)	0.855	-

Equation (10) solves the base fluid thermal conductivity as a function of temperature:

$$k_{bf} = -6.58\times10^{-6}T^2 + 0.0018T + 0.5694 \quad (10)$$

6. Boundary Conditions

Table 3 indicates non-dimensional boundary conditions used for solving the governing equations [32].

7. Evaluation Parameters

The Nusselt number (Nu) and pressure drop coefficient, as the fundamental parameters to study flow behaviour, are calculated as follows [34]:

$$Nu(z^*) = 1\Big/\left(T_w^*(z^*) - T_{bulk}^*(z^*)\right) \quad (11)$$

T^*_w (z^*) and T^*_{bulk} (z^*) are nondimensionalized *wall* temperature and *bulk* temperature, where the *bulk* temperature is:

$$T_{bulk}^*(z^*) = \left(\iint V_z^* T^* dx^* dy^*\right)\Big/\left(\iint V_z^* dx^* dy^*\right) \quad (12)$$

$$Nu = \frac{1}{L^*}\int_0^{L^*} Nu(z^*)dz^* \quad (13)$$

$$f = P_{in}^* - P_{out}^* \Big/ 5(\mathrm{Re\,Pr})^2 \quad (14)$$

The thermal performance, which is known as performance evaluation criteria (*PEC*) and secondary flow intensity (I_{sec}), is defined below [34]:

$$PEC = \left(Nu/Nu_0\right)\Big/\left((f/f_0)^{1/3}\right) \quad (15)$$

$$I_{\sec} = \sqrt{V_x^{*2} + V_y^{*2}}\Big/\left(\mathrm{Re.Pr}\right) \quad (16)$$

The nondimensional total entropy generation, due to heat transfer (S^*_T) and friction (S^*_f), is computed locally as follows [37]:

$$S_{gen}^* = S_T^* + S_f^* = \left(k_{ff}/k_{bf}\right)\left(|\nabla^* T^*|^2/(T^* + 1/q^*)^2\right) + \left(\mu_{ff}/\mu_{bf}\right)\mathrm{Ec.Pr}\left(\phi_v^*/\left(T^* + 1/q^*\right)\right) \quad (17)$$

8. Size Independence

Figure 3 presents the structured hexahedral computational mesh employed in this study. Local refinement was applied near the vortex generators and channel walls to accurately capture steep gradients, while coarser elements were used in uniform flow regions. A grid independence test was performed using four different grid densities (α=45°, Re = 1000, and Mn=1010), with the corresponding results summarized in Table 4 for the average Nusselt number and pressure drop coefficient.

Table 3. Nondimensional form of boundary conditions.

Boundary	**Mathematical expression**
Inlet	$V_x^* = V_y^* = 0,\ V_z^* = \mathrm{Re.Pr},\ T^* = 0$
Outlet	$\partial V_x^*/\partial z^* = \partial V_y^*/\partial z^* = \partial V_z^*/\partial z^* = 0,\ \partial^2 T^*/\partial z^{*2} = 0$
Bottom Wall	$V_x^* = V_y^* = V_z^* = 0,\ \partial T^*/\partial y^* = -\,k_{bf}/k_{ff}$
Upper Wall	$V_x^* = V_y^* = V_z^* = 0,\ q^* = 0$
Side Walls	$\partial\psi^*/\partial x^* = 0;\ \psi^* = V_x^*, V_y^*, V_z^*, T^*, P^*$

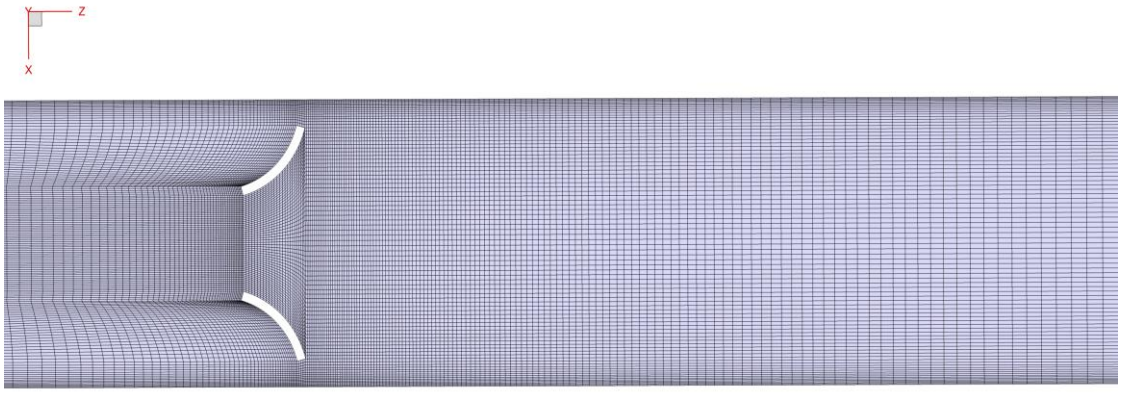

Fig.3. Structured mesh for the channel featuring a concave VG

Table 4. Changing the average Nusselt number and friction factor for grid independence

Grid	Cells	Nu	RE%	f	RE%
1	900,000	59.76	-	0.546	-
2	1,150,000	59.03	1.22	0.539	1.28
3	1,300,000	58.53	0.85	0.537	0.53
4	1,450,000	58.00	0.90	0.535	0.37

It was observed that refining the mesh from 1,300,000 to 1,450,000 cells reduced the relative error of both parameters to below 1%. Therefore, the third grid configuration was selected and applied to all subsequent simulations. The relative error can be calculated as follows:

$$RE = \left(X_i \Big/ X_{i+1} - 1 \right) \times 100 \tag{18}$$

9. Validation

To validate the CFD codes, the current study was carefully compared with similar published studies in the literature. Initially, the variation of the local Nusselt number was compared with the experimental data reported by [38], as well as with the present numerical results for ferrofluid heat transfer in a pipe. As shown in Fig. 4-a, the average deviation is around 3%, demonstrating a strong correlation between the datasets. Subsequently, a second comparison was carried out using numerical results related to mixed convective heat transfer of magnetic fluids in a vertical annulus exposed to a linear magnetic field. As illustrated in Fig. 4-b, the current findings show acceptable consistency with the results of [39] and [40]. The third validation step involved comparing the present numerical results with experimental data concerning fluid flow in a channel equipped with a pair of rectangular VGs, as presented by [41]. Figure 4-c highlights this comparison, confirming excellent agreement between the two sets of results. Finally, the Nusselt number distribution along a channel with rectangular VGs was compared to the numerical findings of [42]. As depicted in Fig. 4-d, the current results align well with the referenced data, further validating the accuracy of the numerical approach.

Furthermore, the validity of the numerical model is compared by [43], who examined a non-Newtonian fluid flow through a 2D channel subjected to a current-carrying wire. The streamline pattern for Re=250 and Mn=315 is illustrated in Fig. 5 and shows good consistency and accuracy.

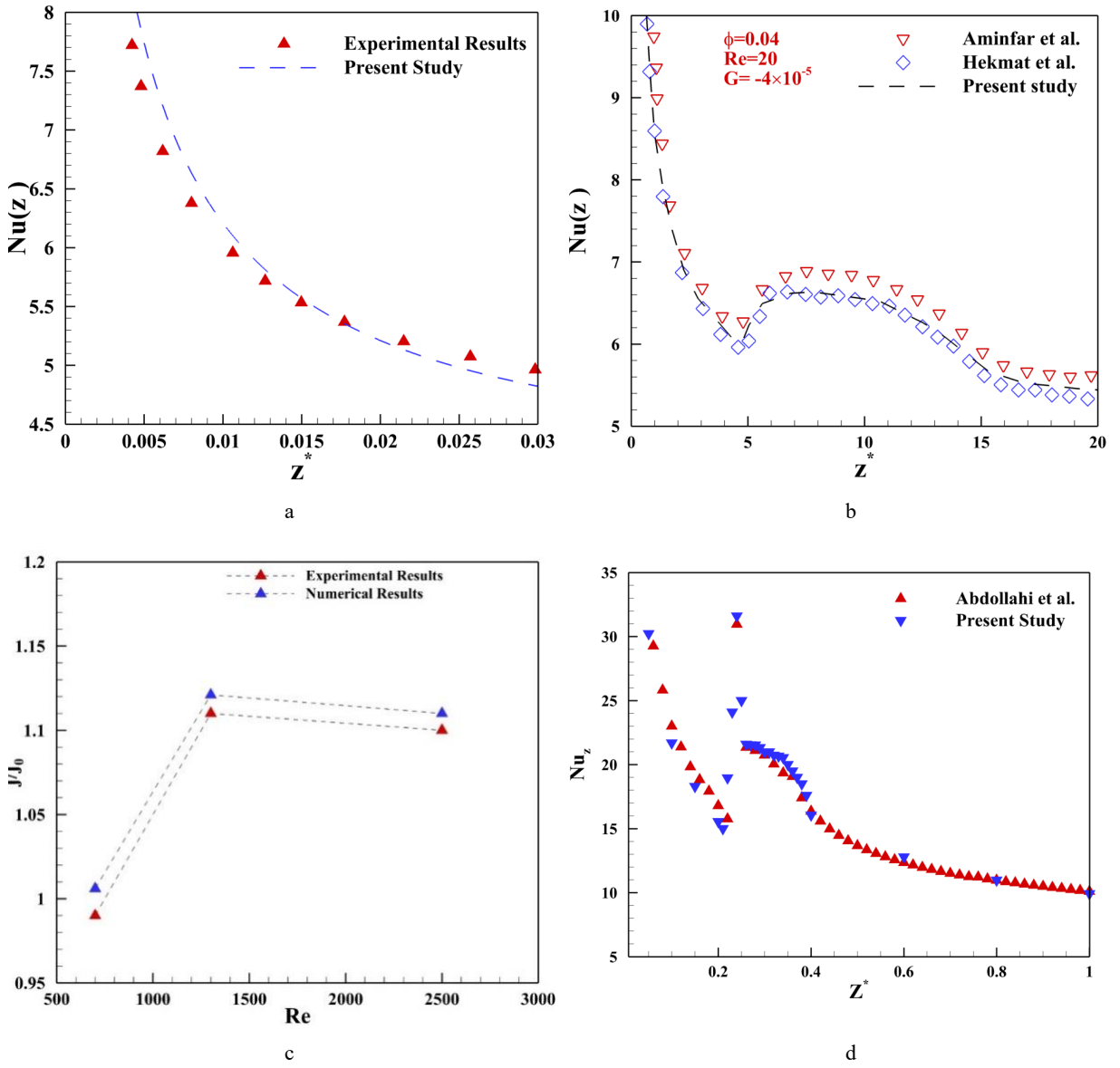

Fig. 4. a) Comparison of the local Nusselt number between the present results and experimental data b) Comparison of the local Nusselt number between the current study and existing numerical results c) Evaluation of the Nusselt number in a channel with a rectangular VG against experimental findings d) Validation of the local Nusselt number for channel flow incorporating a rectangular VG

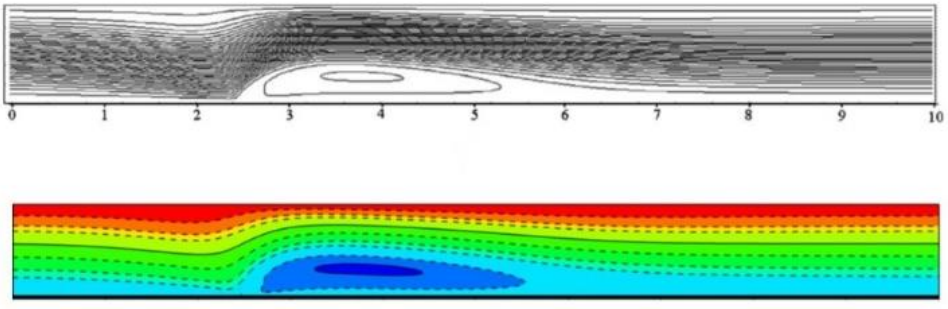

Fig. 5. Streamline comparison for a non-Newtonian fluid subjected to an MF.

10. Results

The results section discusses the effects of the concave VG, Re, α, and Mn in two parts, including thermal and entropy analysis. This study investigates five Magnetic numbers ($0 \leq Mn \leq 10^{10}$), three Reynolds numbers (500, 750, and 1000), and three α (20^{o}, 30^{o} and 45^{o}).

10.1. Thermal Analysis

To investigate the thermal performance of the heat exchanger, the effects of the parameters mentioned are studied, as well as heat transfer, pressure drop, and performance evaluation criteria. To this end, the results are presented in detail below.

10.1.1. Magnetic Number Effect (Mn)

The effect of increasing the Mn as one of the parameters affecting the flow structure and thermal performance of a heat exchanger with a concave VG at Re = 1000 and α = 45° is investigated locally in Fig. 6.

Figure 6a illustrates the variation of streamlines at the outlet. In the absence of the MF (Mn = 0), two large vortex pairs appear across the channel cross-section, formed by the VGs. When the MF is applied, the interaction between the VG-induced vortices and those generated by the MF alters the flow structure, causing the large vortex pair near the periodic regions to deform into two smaller corner vortices ($Mn = 2.5\times10^{9}$). As the MF intensity increases, these corner vortices become stronger and larger, such that at $Mn = 10^{10}$, both vortex pairs attain nearly identical sizes.

Figure 6-b illustrates that the corner vortex pair is initially much stronger than the central one. However, upon applying the MF, the interaction between the vortices induced by the VG and those generated by the MF enhances the strength of the central vortices, making them dominant over the corner vortex pair. This indicates that the central vortices induced by MF play a governing role in the flow, and through their synergistic interaction with the vortices generated by VG, they suppress the influence of the corner vortex pair.

Figure 6-c shows that at Mn = 0, a high-velocity region forms at the channel center, while the dominant corner vortices reduce the axial velocity in their vicinity. With the application and intensification of the MF, the maximum outlet velocity decreases due to enhanced vortex strength, which consequently leads to an improvement in heat transfer.

Figure 6-d demonstrates the beneficial effect of the MF on the temperature field. When the MF is applied at $Mn = 2.5\times10^{9}$, the maximum outlet temperature decreases by about 16% compared to Mn = 0 because of the vorticities generated by MF and its positive interaction with VG's vorticities. As the MF intensity increases to $Mn = 10^{10}$, this reduction reaches approximately 52%, indicating a significant enhancement in the heat transfer rate.

Figure 7 shows the effect of increasing the Mn on the local Nusselt number changes in the x-axis direction at a cross-section of $Z^{*}=0.25$ at Re = 1000 and α = 45 °. Considering the location and intensity of the central vortex pair as shown in Figures 6-a and b, the changes in the local Nusselt number indicate that the effect of the central vortex pair and its positive interaction with the corner vortices has led to an increase in heat transfer.

10.1.2. Vortex Generator Effect (VG)

In this section, the effects of different flow control strategies on the velocity and temperature fields are examined. First, the influence of the MF in a plain channel (without the VG) is analyzed. Next, the performance of the channel equipped with a VG without the MF is compared with that of the magnetically actuated channel. Finally, the combined impact of both methods on the flow field is investigated.

Figure 8 shows the changing axial velocity along the channel at the cross-sections due to the MF and VG when Re = 1000 and $Mn = 7.5\times10^{9}$. Figure 8-a shows that in a plain channel, the constant MF maintains stable high-velocity regions after Z* = 0.25. In a channel with VG (Mn = 0), Fig. 8b illustrates high-velocity zones forming behind the VGs due to vortex generation, which gradually weaken toward the outlet as flow inertia decreases. When VGs and the MF are combined, Fig. 8c shows a synergistic effect: the MF reinforces the secondary flow, sustaining vortex strength along the channel despite the reduction in flow inertia.

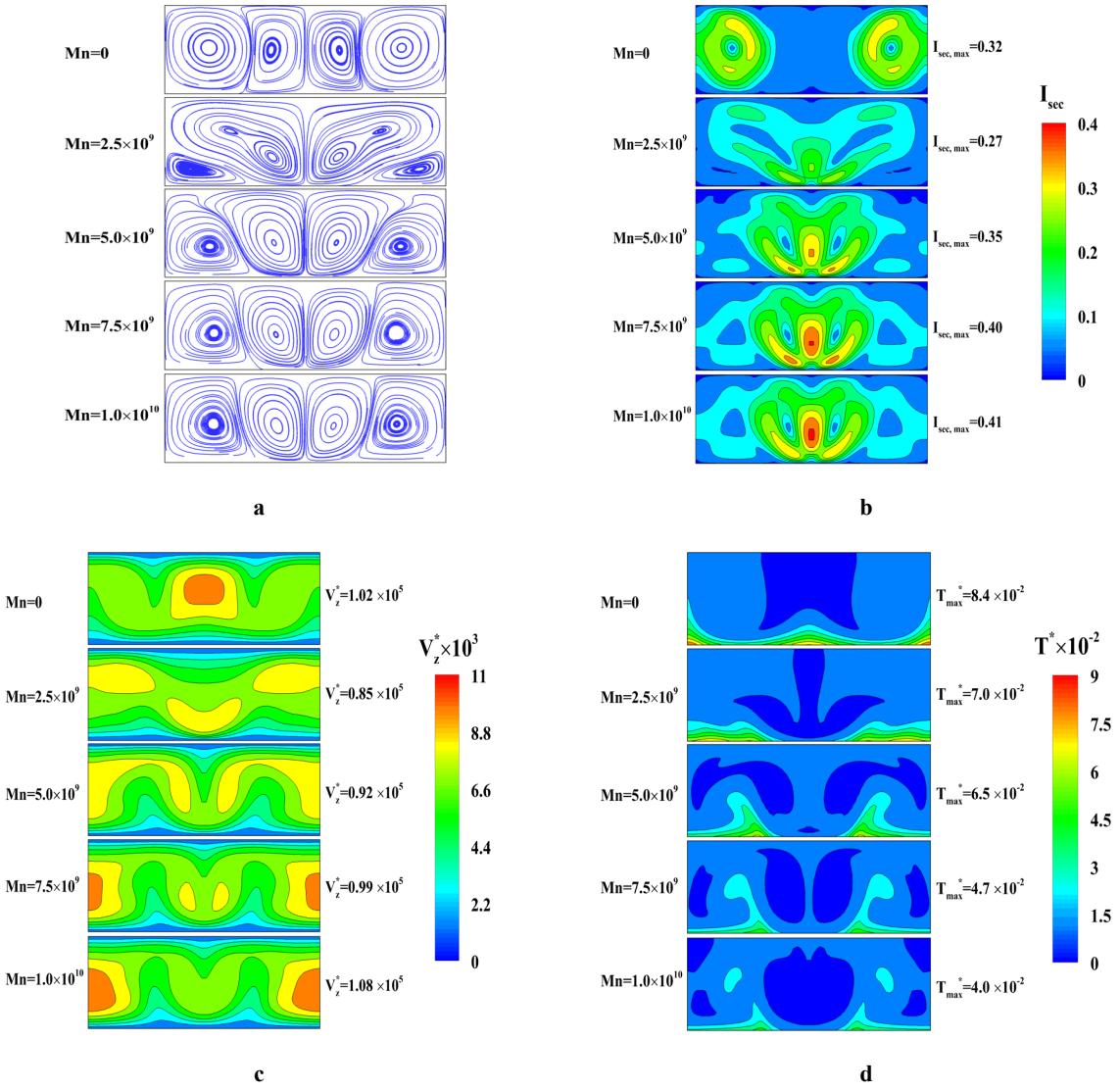

Fig. 6. Comparison of the effect of Mn on a) Streamline pattern, b) secondary flow intensity, c) Axial velocity, and d) Temperature field for Re=1000 at the outlet section.

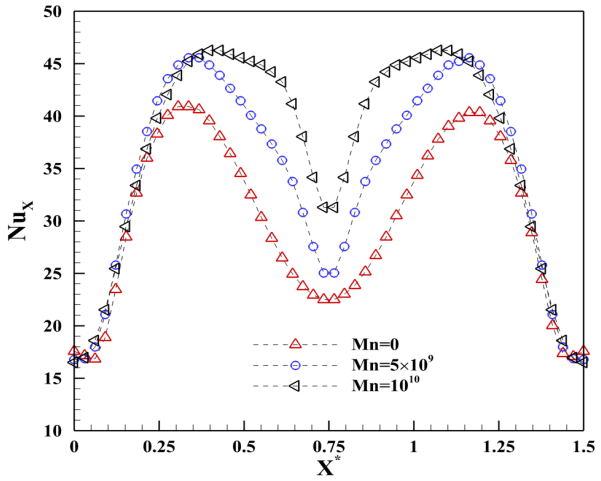

Fig. 7. Comparison of the effect of increasing MF intensity on local Nusselt number for Re=1000 at Z^*=2.5

Figure 9 illustrates the temperature field evolution along the channel. In a plain channel, applying the MF enhances flow mixing and heat transfer by creating a temperature gradient (Fig. 9a). With VGs independently, strong local temperature gradients form behind the VGs due to intense secondary vortices, boosting local heat transfer (Fig. 9b). When VGs and the MF are combined, their vortices interact positively, producing a more uniform temperature gradient along the channel and further enhancing overall heat transfer (Fig. 9c).

Figure 10 illustrates the individual and combined effects of the VG and MF on the local Nusselt number at Z* = 0.25. When the MF is applied to the channel without a VG, heat transfer increases near the current-carrying wire due to the aligned rotation of induced vortices. In the presence of the VG without the MF, a stronger enhancement occurs because of intensified secondary flows. When both methods are applied together, the MF positively interacts with the vortices generated by the VG and amplifies them, further improving heat transfer. Overall, the VG and MF cause about 140% and 30% enhancement, respectively, while their simultaneous application results in a 160% improvement.

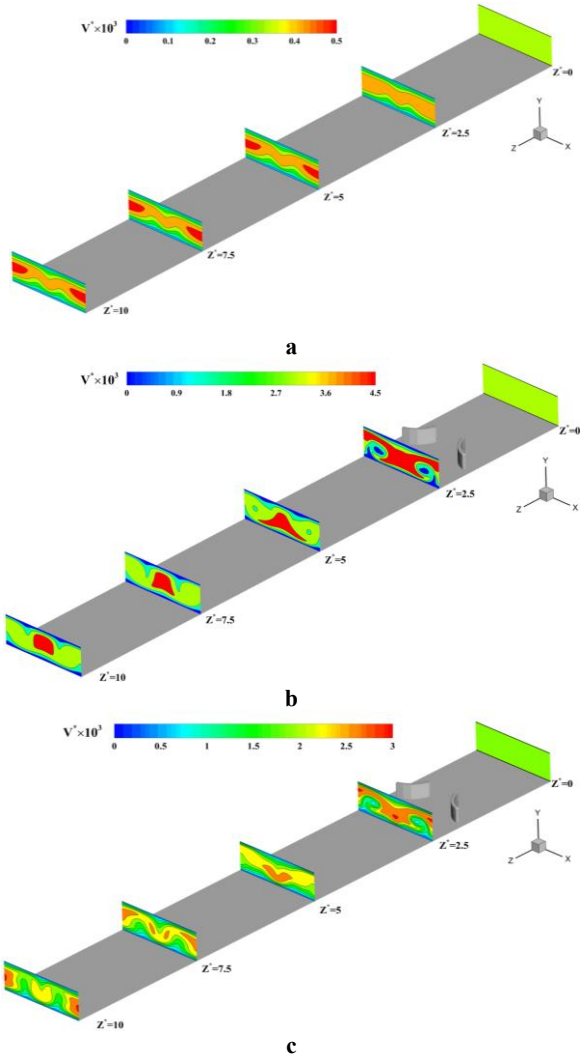

Fig. 8. Comparison of the effect of a) MF when Mn=7.5×10^9 (without VG), b) VG (Mn=0), and c) simultaneous use of VG and MF (Mn=7.5×10^9) on the axial Velocity distribution

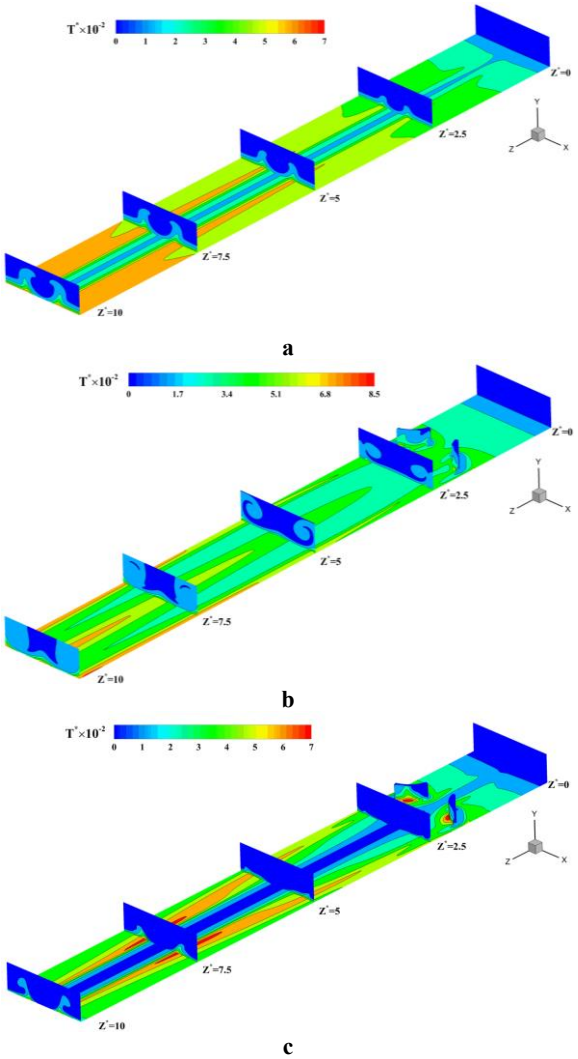

Fig. 9. Comparison of the effect of a) MF when Mn=7.5×10^9 (without VG), b) VG (Mn=0), c) simultaneous use of VG and MF (Mn=7.5×10^9) on the Temperature field distribution

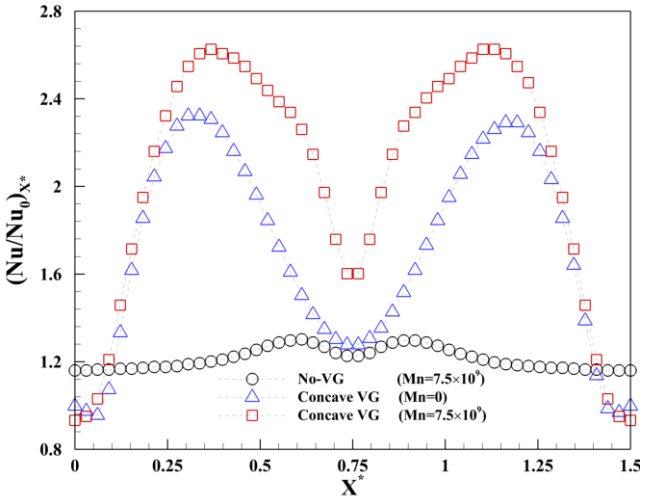

Fig. 10. Comparison of the effect of the MF (without VG), VG (Mn=0), and simultaneous use of VG and MF on Local Nusselt Number at Z*=2.5

Figure 11 illustrates the impact of the concave VG and Mn augmentation on Nu/Nu_0, f/f_0, and PEC and compares these results with those of the channel without the VG. In general, inducing a secondary flow increases the heat transfer rate and pressure drop through enhanced mixing and increased friction, respectively, which vary depending on the intensity of the secondary flow, influenced by the vortices induced by the vVG and the strength of the MF. Accordingly, increasing the Mn in both channels increases the Nu/Nu_0 and f/f_0. In the channel with concave VG, by strengthening the vortices caused by the VG with the magnetic field, the flow mixing rate and friction coefficient have increased significantly compared to the channel without the VG, which has led to increased Nu/Nu_0 and f/f_0. The highest Nu/Nu_0 and f/f_0 values were obtained at $Mn=10^{10}$, respectively, equal to 184% and 215%. Furthermore, using concave VG independently (Mn=0) resulted in a maximum increase of 39% and 57% in Nu/Nu_0 and f/f_0, respectively. In addition, the comparison of PEC shows that the channel with VG and without VG had an optimum point at $Mn=7.5\times10^9$.

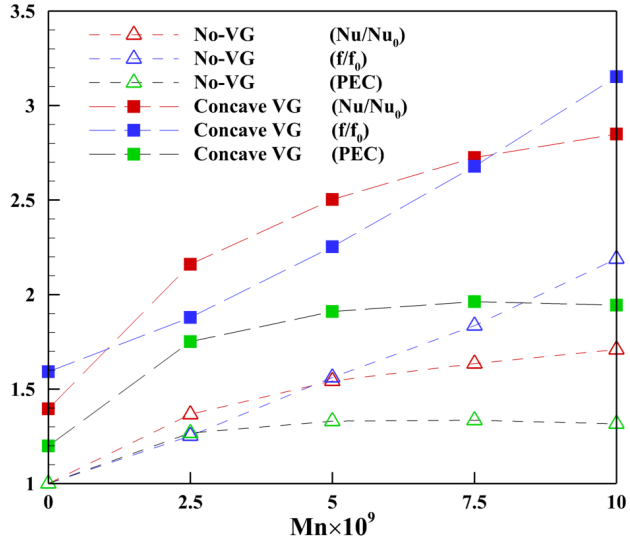

Fig. 11. The effect of VG and MF on Average Nusselt number, Pressure drop coefficient, and Performance evaluation criteria

10.1.3. Reynolds Number Effect

The impact of increasing flow inertia by raising the Reynolds number (Re) on the heat exchanger's thermal performance was investigated using three Re values to analyze the velocity field, temperature field, and secondary flow intensity, as shown in Fig. 12. As shown in Fig. 12-a, increasing the Re at Mn = 10^{10} causes a reduction in the effect of Kelvin force on ferrofluid flow and enhances and expands the high-speed regions at the outlet, increasing the maximum axial velocity from 4900 to 9000. This rise in inertia weakens the MF effects, reducing both heat transfer and pressure drop. Figure 12-b shows that the temperature gradient intensifies with the Reynolds number, further diminishing flow mixing due to the dampened MF influence. Similarly, Fig. 12-c illustrates a drop in secondary flow intensity due to the domination of inertia over the MF effect at the outlet, decreasing from 0.8 to 0.3.

Figure 13 illustrates how increasing the Re affects the average heat transfer rate, pressure drop coefficient, and thermal performance. As shown in Fig. 13-a, at a constant Mn, higher Re reduces heat transfer due to the suppression of MF effects by flow inertia. Conversely, at a constant Re, increasing Mn enhances heat transfer by strengthening MF-induced secondary flows. Notably, when Mn = 0, heat transfer improves with rising Re because of an augmentation in flow inertia.

The increase in pressure drop with rising Re is mainly attributed to the higher flow velocity, which intensifies wall shear stress and frictional resistance along the channel. As Re increases, the momentum of the fluid grows, leading to stronger velocity gradients near the wall and consequently greater energy loss due to viscous effects. Figure 13-b shows that at Mn = 0, the highest pressure drop occurs at Re = 1000. However, with the application of the MF up to Mn = 5.0×10^{9}, pressure drop coefficients converge across all three Reynolds numbers. At a specific Re, increasing the Mn increases the MF effect on the ferrofluid flow, counteracting the inertial effects to some extent. This makes the MF effect more noticeable at lower Re. This is why the pressure drop is higher at lower Re for Mn>5×10^{9}. Overall, the highest heat transfer (215%) and pressure drop (236%) occur at Re = 500 and Mn = 10^{10}.

As shown in Fig. 13-c, the performance coefficient is highest at Re = 500 due to enhanced heat transfer, with Mn = 7.5×10^{9} identified as the optimal point across all Re values.

10.1.4. Angle of Attack Effect (α)

The effect of increasing the α of the VG on the velocity, temperature, and secondary flow intensity fields is investigated in Fig. 14. Based on the results of the previous sections, the performance coefficient was higher at Re = 500. For this reason, Re = 500 was used in this section to evaluate the impact of increasing the α.

In a channel with concave vortex generators, the application of a magnetic field introduces an additional Kelvin force that interacts with the ferrofluid flow .

Increasing the angle of attack, as shown in Figure 14-a, intensifies flow separation and vortex formation behind the VG, resulting in stronger recirculation zones and higher velocity gradients near the wall. By increasing the angle of attack, the vortices generated by VG will be more intensified by the MF through stabilizing the rotational motion of the induced vortices.

As a result, the velocity field exhibits stronger and more coherent vortical structures, particularly near the VG and the regions close to the current-carrying wire. The temperature field becomes more uniform due to enhanced mixing and higher convective transport, leading to a thinner thermal boundary layer and improved wall heat transfer (Fig. 14-b).

The secondary flow field also strengthens noticeably, since the magnetic field reinforces the swirling motion generated by the VG, increasing transverse momentum exchange. However, at larger attack angles, the combined effects of stronger vortices and magnetic forces can raise flow resistance and pressure drop, even though heat transfer performance continues to improve up to an optimal point (Fig. 14-c).

Figure 15-a illustrates that increasing the VG's α enhances the Nusselt number across all

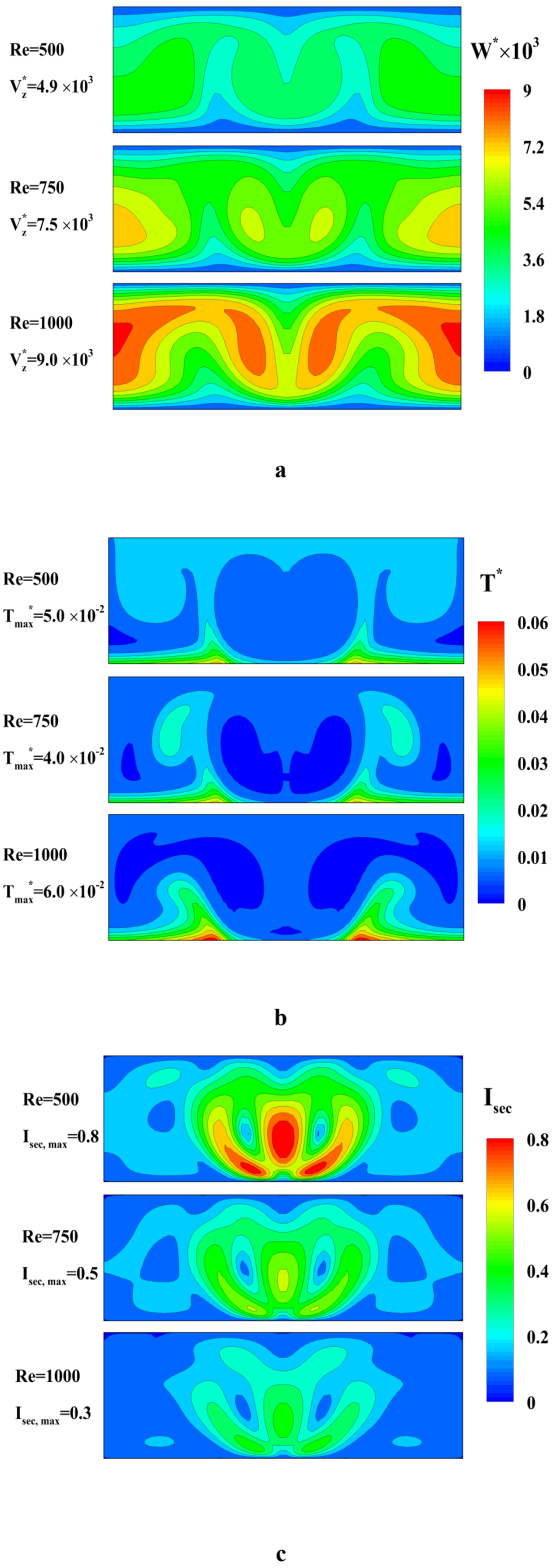

Fig. 12. Comparison of the effect of Re on a) Axial velocity, b) Temperature field, c) Secondary flow intensity for Mn=10^{10}

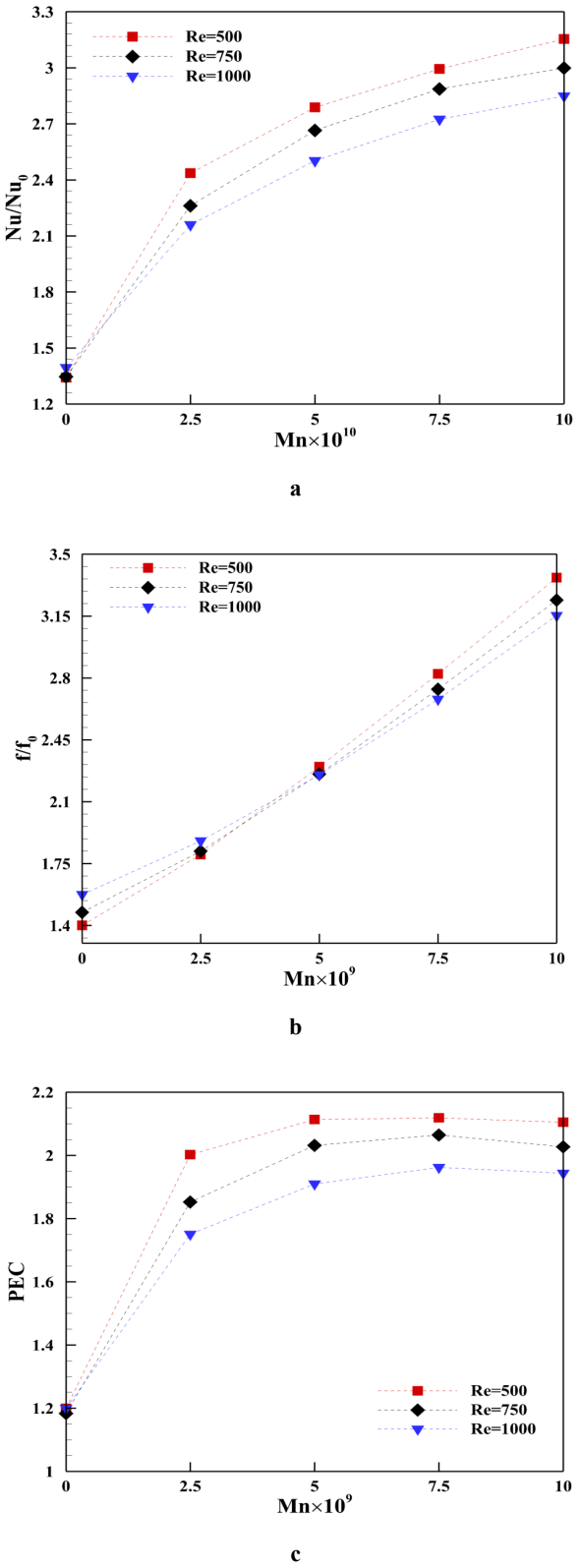

Fig. 13. The effect of Re on a) Average Nusselt number, b) Pressure drop coefficient, c) Performance evaluation criteria for different MF intensity

Mn values due to stronger vortex formation.

Even at Mn = 0, heat transfer rises with angle, reaching a 34% increase; at Mn = 10^{10}, it peaks at 215%. Figure 15-b shows that the pressure drop also increases with α, regardless of Mn. The maximum pressure drop is 40% at Mn = 0 and 236% at Mn =10^{10}. As shown in Fig. 15-c, the performance coefficient reaches its highest value at Mn =7.5×10^{9} across all angles, with the optimum occurring at a 45° angle.

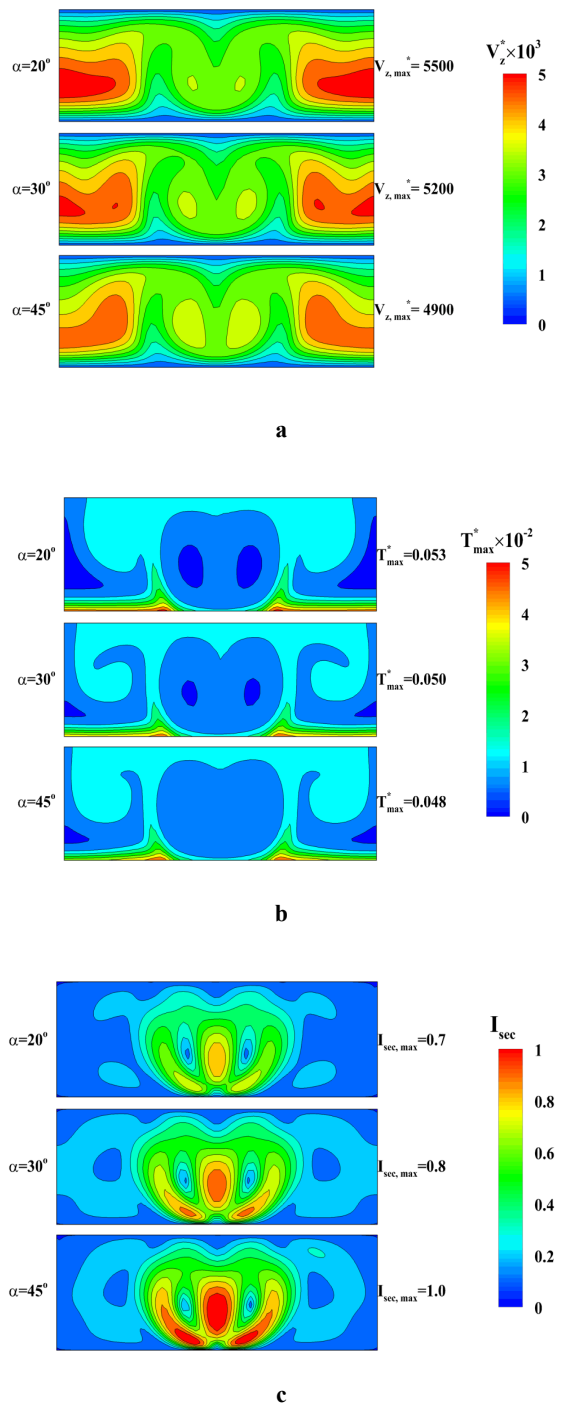

Fig. 14. Comparison of the effect of α on a) Axial velocity, b) Temperature field, and c) Secondary flow intensity for Mn=1010 at the outlet section

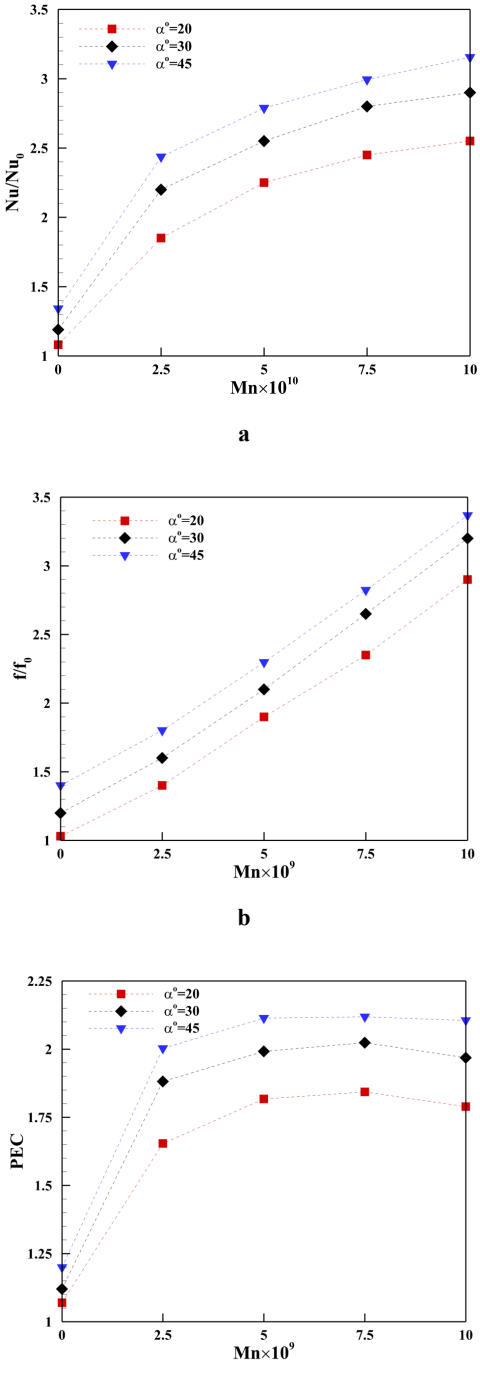

Fig. 15. The effect of α on a) Average Nusselt number, b) Pressure drop coefficient, c) Performance evaluation criteria for different MF intensity

10.2. Entropy Analysis

Entropy production analysis is essential for evaluating thermal system performance based on the second law of thermodynamics. Figure 16 examines total entropy production due to heat transfer and friction, considering the effects of the VG, Re, Mn, and α. As defined by Equation 17, lower entropy production indicates improved system performance. While increased heat transfer reduces entropy production, higher pressure drop raises it, making enhanced heat transfer beneficial and increased pressure drop undesirable.

Figure 16-a shows that at Re = 1000 and Mn = 0, using the VG reduces total entropy production by 14%. In the VG-free channel, applying the MF between Mn = 2.5×10^{9} and 7.5×10^{9} decreases entropy production due to dominant heat transfer effects, reaching a minimum at Mn = 7.5×10^{9}. However, at Mn = 10^{10}, the rising pressure drops increase entropy production. In the presence of the VG, at Mn = 2.5×10^{9}, the entropy generation is reduced by 26% compared to the channel without VG (Mn=0), but further increases in Mn lead to higher entropy due to pressure effects, making Mn = 2.5×10^{9} the optimal point.

Figure 16-b illustrates the effect of increasing the Re on total entropy production. In the absence of an MF, increasing the Re reduces total entropy generation by about 10%, as heat transfer irreversibilities dominate over frictional effects. Moreover, for all Re, total entropy generation reaches a minimum at a specific Mn before rising again. This increase indicates that, after this point, more energy is dissipated to overcome frictional resistance, making pressure drop the main contributor to irreversibility. Consequently, as flow inertia increases, the minimum total entropy generation occurs at lower Mn. Overall, the lowest total entropy production for Re = 500 at Mn = 7.5×10^{9} is 2.44×10^{-5}, which is a 44% decrease compared to the base model (Mn = 0 and No-VG).

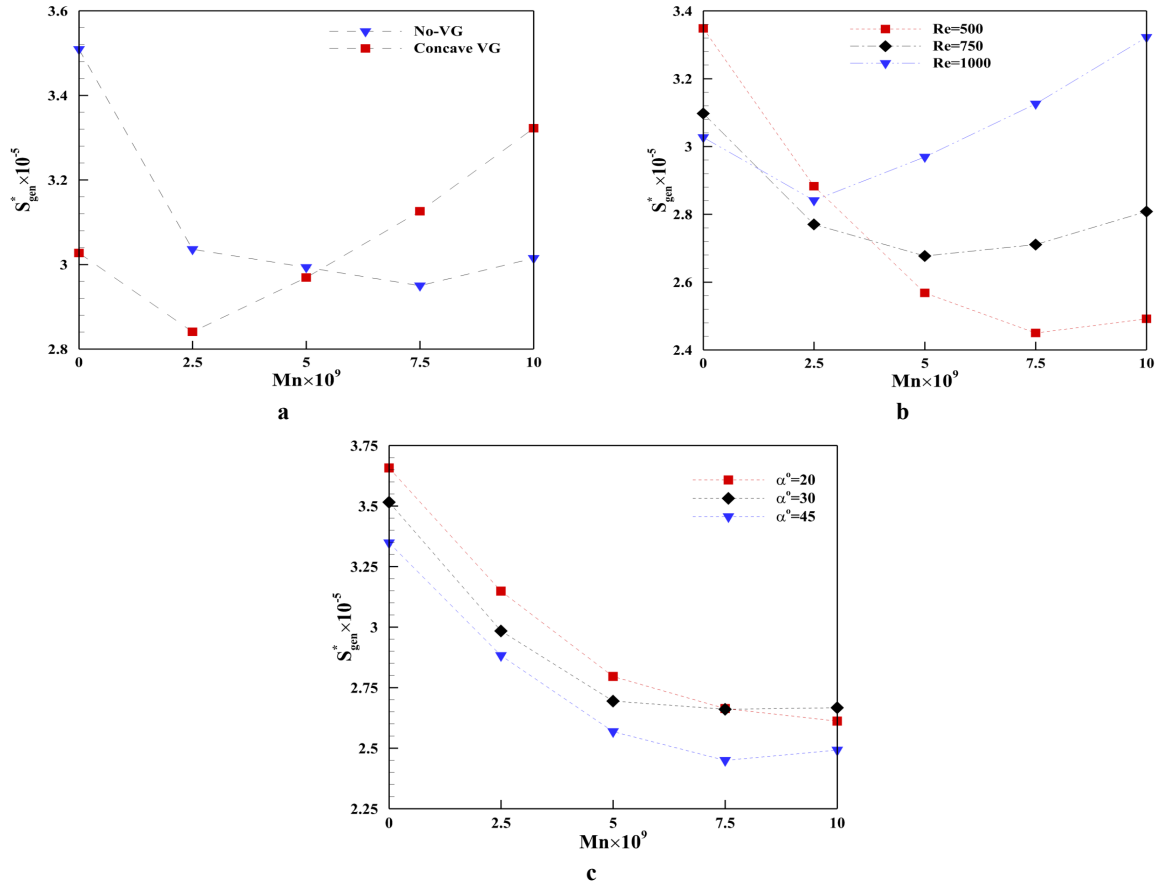

Fig. 16. Comparison of the effect of a) VG, b) Re number, and c) α on Total Entropy Generation for different Mn

In the Mn range of 0 to 5×10^9, increasing the α consistently reduces total entropy generation, indicating that heat transfer irreversibilities dominate over frictional effects. At Mn = 7.5×10^9, the total entropy generation values at 20° and 30° are nearly identical, while at 45°, the stronger secondary flow induced in the ferrofluid maintains the dominance of heat transfer irreversibilities over pressure drop. Under this condition, the minimum total entropy generation of 2.45×10^{-5} is achieved. Overall, increasing the α to 45° at Mn = 7.5×10^9 results in a 43% reduction in total entropy generation compared to the base model.

The changes in the total entropy production field at the channel's outlet are based on the increase in Re, Mn, and α, which are shown in Fig. 17. These changes show that applying the MF at a given Re increases the total entropy production gradient in the areas close to the current-carrying wire. Also, increasing the MF intensity at certain α leads to a similar result. In addition, it is clear that at Mn = 0, the total entropy production rate at the channel outlet has decreased with increasing Re and α. However, when Mn ≠ 0, it cannot be accurately determined by increasing the Reynolds number and α whether the entropy production is less or more than in the other case.

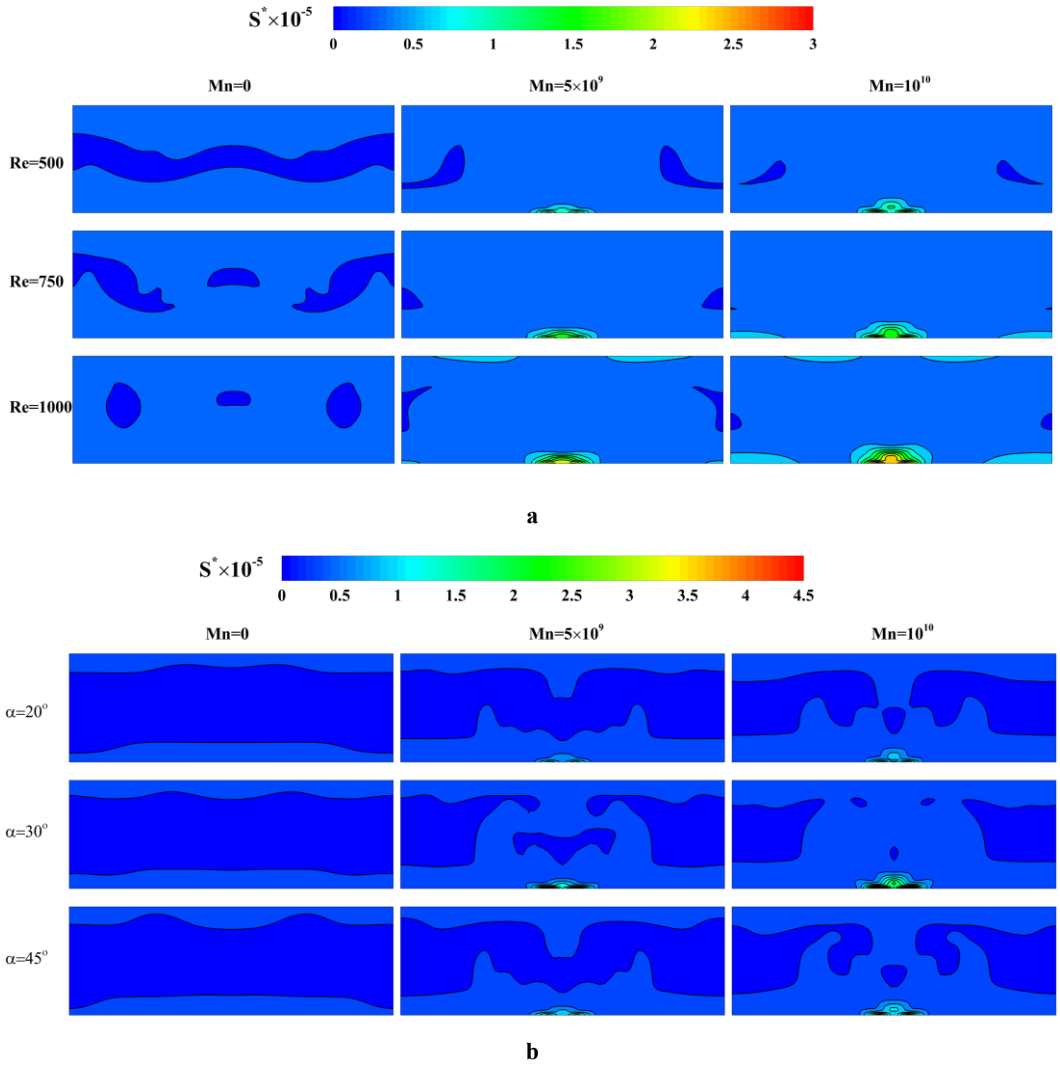

Fig. 17. The effect of increasing a) Re and Mn numbers, b) α and Mn number on Total Entropy distribution at the outlet section

11. Conclusion

This study numerically investigated the flow control methods on thermal performance, flow structure, and entropy generation in a 3D plate heat exchanger. The analysis focused on the simultaneous application of a concave VG as a passive flow control method and an MF as an active technique to enhance thermal performance and reduce entropy generation. The novelty lies in exploring their combined influence in steady laminar ferrofluid flow, an area rarely addressed in previous studies. Key parameters, including Re (500, 750,1000), Mn (0-10^{10}), and VG's α (20, 30, 45), were systematically varied to evaluate their effects on flow structure, Nusselt number, pressure drop, performance evaluation criteria (PEC), and entropy generation. The comprehensive CFD-based assessment provides valuable insights into synergistic heat transfer enhancement and irreversibility minimization in compact heat exchangers. In this regard, in the following, the main results of this research are provided:

- The combined application of the VG and MF demonstrates a positive synergistic effect, where the vortices induced by the VG are enhanced under the MF, leading to an intensified secondary flow.
- Local Nusselt number variations near the VG reveal that the combined effect of the VG and MF is primarily governed by the intensity of the vortices induced by the VG.
- Analysis of the flow structure reveals that applying the MF to a channel with a VG intensifies the secondary flow primarily in the central regions. This occurs because the vortex pairs formed in the middle of the channel are stronger than those near the corners, leading to an increased temperature gradient.
- Since the MF is constant along the channel length, the inertial effects reduce as the fluid flow approaches the outlet, leading to decreased temperature gradients and lower heat transfer rates.
- Thermal performance analysis shows that the individual effect of the VG with α = 45° at Mn = 0 has the highest heat transfer rate and pressure drops of 39% and 57%.
- The use of VG and MF at the same time has increased the Nu/Nu_0 and f/f_0 by about 184% and 215%, respectively.
- In general, at constant (non-zero) Mn, increasing the Re weakens the influence of the MF and suppresses the vortices it generates, resulting in a reduced heat transfer rate. In this regard, the highest heat transfer, 215% occurs at Re = 500 and $Mn = 10^{10}$.
- Furthermore, at a constant Mn, increasing the Reynolds number reduces the intensity of the secondary flow, as the flow inertia dampens the effects of the magnetic field.
- Comparison of PEC under varying VG attack angles and vortex strength indicates that, at a constant Re, the channel achieves its maximum PEC at $Mn= 5\times10^9$ and α=45°.
- The combined influence of the VG and MF resulted in a maximum 26% reduction in total entropy production. Given that entropy generation arises from both heat transfer and pressure drop, it can be inferred that at a $Mn = 2.5\times10^9$, the heat transfer effect dominated over the pressure drop.
- Within $5\times10^9 < Mn < 10^{10}$, the lowest entropy generation occurs at Re = 500. For each Reynolds number, entropy generation reaches its minimum at $Mn = 7.5 \times 10^9$, 5.0×10^9, and 2.5×10^9 for Re = 500, 750, and 1000, respectively.

Conflict of Interest

The authors declared no potential conflicts of interest concerning the research, authorship, and publication of this article.

Funding

The authors received no financial support for the research, authorship, and publication of this article.

Data Availability Statements

The datasets generated or analyzed during the current study are available from the corresponding author upon reasonable request.

Acknowledgment

The authors gratefully acknowledge Dr. Hossein Soltanipour, Associate Professor at Urmia University of Technology, for his constructive guidance and technical support in the development and implementation of the UDF code.

References

[1] Joshi SN, Gujarathi YS. A review on active and passive flow control techniques. International Journal on Recent Technologies in Mechanical and Electrical Engineering. 2016;3(4):1-6.https://doi.org/10.1007/s10973-021-11168-5

[2] Sheikholeslami M, Ganji DD. Ferrohydrodynamic and magnetohydrodynamic effects on ferrofluid flow and convective heat transfer. Energy. 2014;75:400-10.https://doi.org/10.1016/j.energy.2014.07.089

[3] Motlagh SY, Soltanipour H. Natural convection of Al2O3-water nanofluid in an inclined cavity using Buongiorno's two-phase model. International Journal of Thermal Sciences. 2017;111:310-20.https://doi.org/10.1016/j.ijthermalsci.2016.08.022

[4] Awais M, Bhuiyan AA. Heat transfer enhancement using different types of vortex generators (VGs): A review on experimental and numerical activities. Thermal Science and Engineering Progress. 2018;5:524-45.https://doi.org/10.1016/j.tsep.2018.02.007

[5] Ebrahimi A, Rikhtegar F, Sabaghan A, Roohi E. Heat transfer and entropy generation in a microchannel with longitudinal vortex generators using nanofluids. Energy. 2016;101:190-201.https://doi.org/10.1016/j.energy.2016.01.102

[6] Mali AK, Jana T, Kaushik M, Choubey G. A survey on control techniques to augment compressible jet mixing. Flow, Turbulence and Combustion. 2025;114(1). https://doi.org/10.1007/s10494-024-00588-6

[7] Karthikeyan K, Harish R. Enhanced aerodynamic performance of NACA4412 airfoil through integrated plasma actuator and Gurney flap flow control. Results in Engineering. 2025;25.https://doi.org/10.1016/j.rineng.2025.103977

[8] Nabhani A, Tousi NM, Coma M, Bugeda G, Bergadà JM. Large-scale horizontal axis wind turbine aerodynamic efficiency optimization using active flow control and synthetic jets. Energy. 2025.https://doi.org/10.1016/j.energy.2025.134940

[9] Sun Y, Qian Y, Wang T, Wang L, Zhu C, Gao Y. Quantitative impact of combining blowing and suction flow control on a floating offshore wind turbine aerodynamic performance under the surge motion. Renewable Energy. 2025;238.https://doi.org/10.1016/j.renene.2024.121945

[10] Lv L, Chen Y, Jiang Y, Wang G, Lu J. Study on effects of magnetic fields of different inhomogeneous on the formation mechanism of microdroplets. Microfluidics and Nanofluidics. 2025;29(1).https://doi.org/10.1007/s10404-024-02780-6

[11] Salehin MN, Saimoon NZ, Ahmed MM, Sarker MRI, Masud MH. Passive flow control devices for road vehicles: A comprehensive review. Engineering Science and Technology, an International Journal. 2025;62.https://doi.org/10.1016/j.jestch.2025.101953

[12] Jia G, Chen C, Wang L, Wang P, Huang B, Wu R. Unsteady hydrodynamic characteristics control of turbine blades by the vortex generators. Ocean Engineering. 2025;324.https://doi.org/10.1016/j.oceaneng.2025.120785

[13] Daugbjerg TS, Crouzier L, Delvallée A, Ogheard F, Pecnik C, Romieu K, et al. Measurement of wettability and surface roughness for metrology and quality control in microfluidics. International Journal of Metrology and Quality Engineering.

2025;16.https://doi.org/10.1051/ijmqe/2024021

[14] Cao Z, Luo L, Yang X, Yan H, Du W. Effects of turning vane on flow control and heat transfer in ribbed two-pass channel with varied rib patterns. International Journal of Thermal Sciences. 2025;207: .https://doi.org/10.1016/j.ijthermalsci.2024.109342

[15] Jamshed S, Tiwari N. Passive control techniques for heat exchangers: Permeability-driven modulation of vortex shedding and heat transfer enhancement. International Communications in Heat and Mass Transfer. 2025;162.https://doi.org/10.1016/j.icheatmasstransfer.2025.108619

[16] Pillai N, Vural E, Flatau A, editors. Active Flow Control Around a Circular Cylinder Using Helmholtz-Type Pulse Combustion. AIAA SCITECH 2025 Forum; 2025.

[17] Huang S, Li Z-W, Peng W-J, Lin J-R, Huang Z-D, Zeng G-Z. Effect of jet flow control in front of the leading bogie on the aerodynamic drag and underbody slipstream of high-speed trains. Engineering Applications of Computational Fluid Mechanics. 2025;19(1).https://doi.org/10.1080/19942060.2024.2447391

[18] Kumar H, Vander Schaaf JC, Islam SAU, Fidkowski K, Bernstein D, editors. Aerodynamic Flow Control Using Active Bleed Actuation with Variable Channel Width. AIAA SCITECH 2025 Forum; 2025.

[19] Dehghan Afifi M, Jalili B, Mirzaei A, Jalili P, Ganji D. The effects of thermal radiation, thermal conductivity, and variable viscosity on ferrofluid in porous medium under magnetic field. World Journal of Engineering. 2025;22(1).https://doi.org/10.1108/WJE-09-2023-0402

[20] Negi AS, Kumar B, Kumar A, Rawat SK, Yaseen M. Investigation of heat flux and heat source/sink effect on heat transfer ferrofluid (CoFe2O4-H2O) flow in an induced magnetic field with porous medium within the horizontal channel. International Journal of Ambient Energy. 2025;46(1).https://doi.org/10.1080/01430750.2024.2447939

[21] Magdy M, Abbas W, Mekheimer KS, Emam M. Ferro-Fluid Flow and Heat Transfer over Unsteady Stretching Sheet in the Presence of a Nonuniform Magnetic Field. Journal of Nonlinear Mathematical Physics. 2025;32(1).https://doi.org/10.1007/s44198-024-00250-9

[22] Wang C, Sui J, Wang X, Zhang X, Liu P, Gong B. Vortex flow properties and enhanced heat transfer analysis of ferrofluid in a curved pipe under the coupling of magnetic field force and centrifugal force. Journal of Mechanical Science and Technology. 2025.https://doi.org/10.1007/s12206-024-1237-z

[23] He M, Zhuang Y, Xu W, Feng J-C. Experimental study on thermal performance regulation of composited phase change system using non-uniform magnetic field generated by a Helmholtz coil. Applied Thermal Engineering. 2025.https://doi.org/10.1016/j.applthermaleng.2025.126081

[24] Ramezani A, Khorasani AF, Ayoobi A. Experimental study on transient pool boiling heat transfer of deionized water under an alternating magnetic field. International Communications in Heat and Mass Transfer. 2025;161.https://doi.org/10.1016/j.icheatmasstransfer.2024.108450

[25] Mansouri SM, Bijarchi MA, Hannani LSKK. The effect of rotating magnetic turbulators on the convective heat transfer and pressure drop through a circular tube: Experimental investigation. International Journal of Thermofluids. 2025;26.https://doi.org/10.1016/j.ijft.2025.101108

[26] Benam BP, Mohammadilooey M, Sadaghiani AK, Çakır E, Acar HY, Park HS, et al. On saturated flow boiling heat transfer of deionized water/ferrofluid on structured surfaces with or without external magnetic field. International Journal of Heat and Mass Transfer. 2025;236.https://doi.org/10.1016/j.ijheatmasstransfer.2024.126323

[27] Liao C-C, Li W-K, Lin H-E. Heat Transfer Enhancement in Microchannel Systems Through Geometric Modification of Vortex Generators and Nanofluid Integration: A Numerical Study. Results in Engineering. 2025.https://doi.org/10.1016/j.rineng.2025.104138

[28] Liang X, Min M, Bian K, Cheng J. Study on the enhanced heat transfer and exergy performance of the finned tube heat exchanger with vortex generator. International Journal of Thermal Sciences. 2025;210.https://doi.org/10.1016/j.ijthermalsci.2024.109639

[29] Ifraj NF, Akter F, Fahad MK, Ahmed DH. Thermal-hydraulic performance enhancement with minimum entropy generation of a heat exchanger using fidget spinner vortex generators. International Communications in Heat and Mass Transfer. 2025;162.https://doi.org/10.1016/j.icheatmasstransfer.2025.108610

[30] Perng S-W, Wu HW, Guo Y-L, Liu T-H. Enhancement of thermo-hydraulic transport within a round tube using a twisted-staggered concave/convex dimples tape. International Journal of Numerical Methods for Heat & Fluid Flow. 2025.https://doi.org/10.1108/HFF-08-2024-0614

[31] Boonloi A, Jedsadaratanachai W. Turbulent forced convection in a square duct heat exchanger (SDHX) equipped with combined vortex turbulators (CVT): A numerical investigation. International Communications in Heat and Mass Transfer. 2025;161.https://doi.org/10.1016/j.icheatmasstransfer.2024.108421

[32] Jalayeri A, Soltanipour H, Rezazadeh S. Simultaneous Effects of a Vortex Generator and Magnetic Field on Ferrofluid Convective Heat Transfer in a 3D Channel: First and Second Law Analyses. AUT Journal of Mechanical Engineering. 2024;8(2).https://doi.org/10.22060/ajme.2024.22788.6075

[33] Rahimi R, Jalayeri A, Soltanipour H, Tahmoresnezhad J. Performance prediction of ferrofluid-actuated double tube heat exchanger using deep neural network based on magnetic field parameters. Applied Thermal Engineering. 2025:128228.https://doi.org/10.1016/j.applthermaleng.2025.128228

[34] Soltanipour H. Numerical analysis of two-phase ferrofluid forced convection in an annulus subjected to magnetic sources. Applied Thermal Engineering. 2021;196.https://doi.org/10.1016/j.applthermaleng.2021.117278

[35] Jalayeri A, Rahimi R. A Comparative Study on Heat Transfer and Entropy Generation of Ferrofluid Flowing Through a Double-Tube Heat Exchanger Subjected to Various Magnetic Fields. International Journal for Numerical Methods in Fluids. 2025.https://doi.org/10.1002/fld.70013

[36] Gavili A, Zabihi F, Isfahani TD, Sabbaghzadeh J. The thermal conductivity of water base ferrofluids under magnetic field. Experimental Thermal and Fluid Science. 2012;41.https://doi.org/10.1016/j.expthermflusci.2012.03.016

[37] Bejan A. Second-law analysis in heat transfer and thermal design. Advances in heat transfer. 15: Elsevier; 1982. p. 1-58.

[38] Asfer M, Mehta B, Kumar A, Khandekar S, Panigrahi PK. Effect of magnetic field on laminar convective heat transfer characteristics of ferrofluid flowing through a circular stainless steel tube. International Journal of Heat and Fluid Flow. 2016;59.https://doi.org/10.1016/j.ijheatfluidflow.2016.01.009

[39] Aminfar H, Mohammadpourfard M, Zonouzi SA. Numerical study of the ferrofluid flow and heat transfer through a rectangular duct in the presence of a non-uniform transverse magnetic field. Journal of Magnetism and Magnetic materials. 2013;327.https://doi.org/10.1016/j.jmmm.2012.09.011

[40] Hekmat MH, Ziarati KK. Effects of nanoparticles volume fraction and magnetic field gradient on the mixed convection of a ferrofluid in the annulus between vertical concentric cylinders. Applied Thermal Engineering.

2019;152.https://doi.org/10.1016/j.applthermaleng.2019.02.124

[41] Zhou G, Ye Q. Experimental investigations of thermal and flow characteristics of curved trapezoidal winglet type vortex generators. Applied Thermal Engineering. 2012;37:241-8.https://doi.org/10.1016/j.applthermaleng.2011.11.024

[42] Abdollahi A, Shams M. Optimization of shape and angle of attack of winglet vortex generator in a rectangular channel for heat transfer enhancement. Applied Thermal Engineering. 2015;81.https://doi.org/10.1016/j.applthermaleng.2015.01.044

[43] Loukopoulos V, Tzirtzilakis E. Biomagnetic channel flow in spatially varying magnetic field. International journal of engineering science. 2004;42(5-6).https://doi.org/10.1016/j.ijengsci.2003.07.007